Numerical Study of Convection in the Directional Solidification of a Binary Alloy Driven by the Combined Action of Buoyancy, Surface Tension, and Electromagnetic Forces

Rajiv Sampath and Nicholas Zabaras

*Sibley School of Mechanical and Aerospace Engineering, 188 Frank H. T. Rhodes Hall,
Cornell University, Ithaca, New York 14853-3801*
E-mail: zabaras@cornell.edu

Directional solidification of a dilute electrically conducting binary alloy driven by the combined action of buoyancy, surface-tension, and electromagnetic forces is considered. A numerical methodology using a moving finite element technique is proposed for the simulation of the above phase change process. The melt is modeled as a Boussinesq fluid and the transient Navier–Stokes equations are solved simultaneously with the transient heat and solute transport equations. The location of the advancing solid–liquid interface is numerically determined using an energy preserving weak form of the Stefan condition. The standard SUPG/PSPG method for the simulation of incompressible fluid flow is here extended to flows driven by the combination of buoyancy, surface tension, and electromagnetic forces. A reference problem of directional solidification of a dilute germanium alloy in a horizontal open-boat configuration is considered. The relative influence of thermocapillary convection and buoyancy-driven convection on the solidification process is investigated by varying the Bond number. Thermocapillary convection is shown to have a significant influence on various solidification parameters, such as the shape of the solid–liquid interface and the solute segregation, especially under low gravity conditions. The influence of an external magnetic field on the reference solidification problem is investigated both in a normal and a reduced gravity environment. It is demonstrated that the application of an appropriate strong magnetic field significantly damps the melt flow and improves the solute segregation pattern. The relative influence of an external magnetic field on the solidification process is also studied by independently varying the orientation and magnitude of the applied magnetic field. © 2001 Academic Press

Key Words: directional binary alloy solidification; Marangoni convection; surface tension; magneto-hydrodynamics; natural convection; finite element method; front tracking methodology; stabilized Navier–Stokes solvers.

1. INTRODUCTION

Convection in the bulk liquid is an important parameter in crystal growth from the melt. A typical driving force for convection in the melt is the buoyancy force induced by thermal and solutal gradients in the liquid. Another driving force for convection, besides buoyancy, is the surface-tension gradient that results from temperature or concentration gradients on a free surface. Surface tension typically decreases with increasing temperature. In a free melt surface with a temperature gradient, surface tension forces drive the flow from regions of low surface tension (hot) to areas of high surface tension (cold). Surface tension forces are balanced by viscous shear which transfers momentum to neighboring liquid layers because of fluid viscosity. Similar to the buoyancy driven flow, continuity causes the development of a bulk flow in the whole melt volume. This convective motion is referred to as Marangoni or thermocapillary convection and occurs if free melt surfaces exist in the growth configuration [1, 2].

The study of Marangoni convection in crystal growth from the melt has proven to be of particular interest with respect to its influence on the distribution of impurities in the obtained crystal structure [3–5]. The role of Marangoni convection becomes quite dominant in reduced-gravity environments. Even under normal gravity, the thermocapillary effect can be very important in the overall transport pattern. A review of various numerical and experimental studies of the interaction of the surface-tension-driven flow and the buoyancy-driven flow in crystal growth melts can be found in [3, 6].

Studies of surface tension effects have concentrated largely on flows without phase change [7–11]. Exceptions include the studies reported in [12–15]. In [12] and [13], the melting and solidification of pure materials was considered, during which liquid convection was driven by a combination of buoyancy and surface-tension forces. In [14, 15], the authors considered the effects of thermo/diffusocapillary convection on the solidification of a binary aqueous solution in a rectangular cavity using a single region (continuum) formulation. Their study showed that surface-tension effects influence significantly the fluid flow and interface morphology during the early stages of the solidification process. It was also observed that the recirculating flow in the melt is stronger, which in turn significantly alters the interface shape. The action of thermocapillary convection on crystal growth processes is generally undesirable because the transition to unsteady behavior is hard to control [16].

Application of magnetic fields is known to stabilize both flow and temperature oscillations in the melt (see Chapters 4 and 7 in [17]) and thereby represents a promising opportunity to obtain an improved crystal quality. The effects of a magnetic field on melt convection have been previously investigated by several authors [18–23]. The effects of a strong vertical magnetic field on convection and segregation in the vertical Bridgman crystal growth process were considered in [20]. More recently, Ben Hadid *et al*. [21–23] have studied the influence of an external magnetic field on convection in a horizontal Bridgman configuration. In [21], an extensive numerical study is presented of buoyancy- and surface-tension-driven convection in a horizontal rectangular cavity under the action of a constant magnetic field. Results of a similar study on a three-dimensional parallelepiped domain are presented in [22]. These formulations dealt purely with the effects of a magnetic field on the fluid flow and did not include the effects of phase-change. In [23], a numerical study was presented of macrosegregation in a horizontal Bridgman configuration under various fluid flow conditions and with the assumption of a planar solid–liquid interface moving at a constant velocity.

In this paper, the complex interaction between solidification and convection for a dilute binary fluid that is crystallized in a rectangular cavity with an open boundary is investigated. A broad range of responses are investigated and reported in a systematic manner by varying the conditions of the relative strength of the driving physical mechanisms under both normal and reduced gravity levels. In the present work, the SUPG/PSPG stabilized FEM for incompressible flows [24, 25] has been extended to a front tracking moving finite element framework appropriate for the analysis of solidification processes. The sharp solid–liquid interface model adopted here is limited to systems with a thin mushy layer and to crystal growth processes with a low growth rate [26]. Even though the applicability of this model is limited, it results in a mathematically tractable framework that can be used to provide a detailed insight into the complex interaction of heat, mass, and momentum transport in the solidification system [27–30]. For materials for which this assumption of a thin mushy zone is not applicable, sharp interface models have been used to pose optimal control problems in which the interface stability is enforced explicitly by a proper selection of the process conditions (e.g., by a boundary heat flux design [31, 32]).

The plan of the paper is as follows. In the following section, the physical problem and the governing equations are defined. Section 3 provides a brief outline of the various solution methods employed to solve the numerical model. Section 4 presents the results of the numerical experiments, wherein the various aspects of the predicted solutions and their implications on the final crystallized solid are discussed. Finally, in Section 5, conclusions are presented based on the various numerical experiments.

2. DIRECTIONAL SOLIDIFICATION OF A BINARY ALLOY IN AN OPEN-BOAT CONFIGURATION IN THE PRESENCE OF A MAGNETIC FIELD

Here, a two-dimensional, rectangular mold Ω is considered filled with a dilute, incompressible, electrically conducting binary alloy which is initially liquid and uniform in temperature and composition (Fig. 1). The top boundary of the box is "free" and subject to temperature induced surface-tension gradients. At time $t = 0^+$, the temperature of the left vertical boundary Γ_{os} is instantaneously dropped and maintained below the freezing temperature corresponding to the bulk concentration of the melt, so that solidification of the
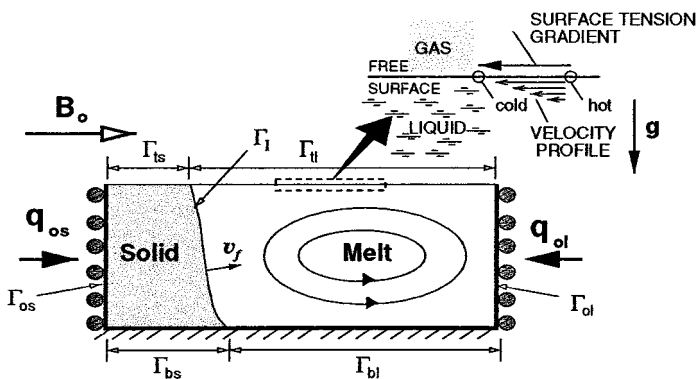

FIG. 1. Schematic of the binary alloy solidification problem in an open-boat configuration under the influence of an externally applied magnetic field.

alloy immediately commences at this "cold" boundary. The motion of the melt is determined by the combined action of buoyancy, surface-tension, and electromagnetic forces.

Let us denote the solid region by Ω_s, the liquid region by Ω_l, and the solid–liquid interface as Γ_I. The region Ω_l has a boundary Γ_l which consists of Γ_I, Γ_{ol} (the mold wall on the liquid side), Γ_{bl} (the bottom boundary of the liquid domain), and Γ_{tl} (the top boundary of the liquid domain). Similarly Ω_s has boundary Γ_s, which consists of Γ_I, Γ_{os}, Γ_{bs}, and Γ_{ts}.

In the solidification system considered in this work, the following assumptions are introduced regarding the transport of heat, mass, and momentum:

- The thermal and physical properties are constant within each phase.
- The solid and liquid phases are in local thermodynamic equilibrium.
- The melt flow is assumed to be a laminar flow induced by thermal, solutal, and surface-tension gradients.
- The Boussinesq approximation can be invoked.
- The solute diffusion in the solid is negligible compared to that in the melt, i.e., $D_s/D_l \to 0$ (D_s and D_l, respectively, are the solid and liquid mass diffusivities).
- Velocities resulting from density change upon phase change are negligible.
- The free-surface deformation is negligible.
- Capillary undercooling resulting from the local curvature of the phase boundary (Gibbs–Thompson effect) is negligible.
- A macroscopically stable solid–liquid interface exists between the solid and the liquid regions.

The above assumptions with the exception of the last three are generally valid for solidification systems with dilute concentration levels, moderate temperature differences, and a Newtonian melt. The assumption that the melt free surface deformation is negligible is strictly valid only at low capillary numbers. This is generally true for metals and semiconductor melts [10]. The Gibbs–Thompson effect is neglected as it is usually important only on very small scales [6, 33]. Finally, the assumption that a sharp solid–liquid interface exists between the solid and liquid domains is quite debatable. Once morphological instability occurs, the perturbations continue to grow to form a two-phase mushy zone in which dendrites are bathed in interstitial melt. Many theoretical models for simulating dendritic solidification processes incorporating a mushy model have been proposed in the recent years [34]. In this paper, however, the simplified model of a sharp solid–liquid interface is adopted to allow us to concentrate on examining the complex interactions of heat, mass, and momentum transport in the solidification system. A number of computational studies have been conducted using the sharp interface model, and the results were found to be on an excellent qualitative agreement with experiments [27–29].

The governing equations for the binary alloy solidification system are now introduced. Let L be a characteristic length of the domain, ρ the density, k the thermal conductivity, α ($\alpha \equiv k/\rho c$) the thermal diffusivity, D the solute diffusivity, σ_e the electrical conductivity, and ν the kinematic viscosity of the liquid melt. All fields and properties refer to the liquid domain unless denoted otherwise. The characteristic scale for time is taken as L^2/α and for velocity as α/L. The temperature θ is defined as $\theta \equiv (T - T_o)/\Delta T$, where T, T_o, and ΔT are the temperature, reference temperature, and reference temperature drop, respectively. Likewise, the dimensionless concentration field c is defined as $(\hat{c} - c_o)/\Delta c$, where $\hat{c}$, c_o, and Δc are the concentration, reference concentration, and reference concentration drop, respectively. The characteristic scale for the electric potential ϕ is taken as $\alpha|\mathbf{B_o}|$, where $\mathbf{B_o}$

is the externally applied magnetic field. Since only dimensionless quantities will be used in the rest of this paper, the symbol ϕ is used hereafter to denote the dimensionless electric potential.

The basic equations used in the simulation of the melt flow are the incompressible Navier–Stokes equations, including the Lorentz force [35]. The Boussinesq approximation is also used for defining buoyancy. The other main equations governing the fluid flow in the liquid domain are the energy equation and the solute transport equation. These equations are written as

$$\nabla \cdot \boldsymbol{v} = 0, \tag{1}$$

$$\frac{\partial \boldsymbol{v}}{\partial t} + \boldsymbol{v} \cdot \nabla \boldsymbol{v} = -\nabla p + Pr\nabla^2 \boldsymbol{v} - [Ra_T Pr\theta_l - Ra_c Prc]\boldsymbol{e_g}$$
$$+ Ha^2 Pr[-\nabla\phi + \boldsymbol{v} \times \boldsymbol{e_B}] \times \boldsymbol{e_B}, \tag{2}$$

$$\frac{\partial \theta_l}{\partial t} + \boldsymbol{v} \cdot \nabla \theta_l = \nabla^2 \theta_l \tag{3}$$

$$\frac{\partial c}{\partial t} + \boldsymbol{v} \cdot \nabla c = Le^{-1}\nabla^2 c, \tag{4}$$

where the governing dimensionless groups are the Prandtl number ($Pr \equiv \nu/\alpha$), the Lewis number ($Le \equiv \alpha/D$), the thermal Rayleigh number ($Ra_T \equiv g\beta_T \Delta T L^3/\nu\alpha$), the solutal Rayleigh number ($Ra_c \equiv g\beta_c \Delta c L^3/\nu\alpha$), and the Hartmann number ($Ha \equiv (\frac{\sigma_c}{\rho\nu})^{1/2}B_o L$), where g is the gravity constant, β_T is the thermal coefficient of expansion, and β_c is the solutal coefficient of expansion. Here, $\boldsymbol{e_g}$ and $\boldsymbol{e_B}$ denote unit vectors in the directions of the gravity and magnetic field vectors, respectively.

Heat transfer in the solid is by conduction and is written as

$$\frac{\partial \theta_s}{\partial t} = R_\alpha \nabla^2 \theta_s, \tag{5}$$

where $R_\alpha \equiv \alpha_s/\alpha_l$ is the ratio of the thermal diffusivities.

The temperature at Γ_I is set by the binary equilibrium phase diagram as

$$\theta = \theta_m + mc, \tag{6}$$

where the dimensionless slope m of the liquidus line is given as $m = m_{liquidus}\Delta c/\Delta T$, $m_{liquidus}$ is the dimensional slope of the liquidus, and θ_m is the dimensionless melting temperature corresponding to the reference concentration.

The energy and solute balances at Γ_I take the form

$$R_k \frac{\partial \theta_s}{\partial n} - \frac{\partial \theta_l}{\partial n} = Ste^{-1}\boldsymbol{v}_f \cdot \boldsymbol{n}, \tag{7}$$

$$\frac{\partial c}{\partial n} = Le\,(\kappa - 1)\boldsymbol{v}_f \cdot \boldsymbol{n}\,(c + \delta), \tag{8}$$

where $R_k \equiv k_s/k_l$ is the ratio of the thermal conductivities of the solid and liquid, $Ste \equiv (C_p\Delta T)/L_H$ is the Stefan number, κ is the partition coefficient, and $\delta \equiv c_o/\Delta c$ is the ratio of the reference concentration c_o and reference concentration drop Δc. In the

above definition, C_p is the heat capacity of the liquid melt, and L_H is the latent heat of solidification.

A no-slip and no-penetration boundary condition on the velocity field is imposed on all the liquid boundaries other than the upper free surface (Fig. 1). The surface tension on the free surface is approximated as $\sigma = \sigma_o[1 - \gamma(T - T_o)]$, where $\gamma = -(1/\sigma_o)(\partial\sigma/\partial T)$. In the present work, the variation of the surface tension with solute concentration is neglected as only minute amounts of solute are considered and hence no appreciable change in surface tension occurs as a result of concentration variation [7]. The hydrodynamic boundary condition on the free surface Γ_{tl} is expressed as

$$\nabla(\mathbf{v} \cdot \mathbf{t}) \cdot \mathbf{n} = Ma(\nabla\theta \cdot \mathbf{t}), \tag{9}$$

where $\mathbf{t}$ is a tangent vector to the free surface, and $Ma \equiv (\partial\sigma/\partial T)\Delta T L/(\rho\nu\alpha)$ is the thermal Marangoni number. Equation (9) is used as a Neumann boundary condition in the solution of the flow equations once the temperature field has been computed. As mentioned earlier, the free-surface deformation is neglected and a no-penetration boundary condition is imposed on the free surface.

It is assumed that adiabatic conditions are maintained on $\Gamma_{bl} \cup \Gamma_{tl}$. The equilibrium condition (see Eq. (6)) imposes a Dirichlet boundary condition on Γ_I. A problem dependent flux/temperature condition on the outer liquid boundary Γ_{ol} completes the definition of the thermal problem defined on Ω_l. The solutal boundary conditions are provided by the impermeable wall condition on the outer boundaries and a flux condition determined by the solute conservation condition (see Eq. (8)) on Γ_I. The electric potential function $\phi(\mathbf{x}, t)$ is governed by an insulating wall condition on the boundary Γ_l.

In the solid phase Ω_s, the equilibrium condition (Eq. (6)) on Γ_I, the problem-dependent flux/temperature condition on Γ_{os}, and the adiabatic conditions on $\Gamma_{ts} \cup \Gamma_{bs}$ (Fig. 1) provide the required boundary conditions for the solution of the heat transport problem. Finally, note that the shape and position of Γ_I are integral parts of the solution of the nonlinear solidification problem.

3. SOLUTION METHODOLOGY AND MODEL VALIDATION

The stabilized finite element formulation using an equal-order velocity-pressure interpolation as proposed by Tezduyar *et al.* [24, 25] is adopted in this work for the fluid flow subproblem. This method achieves stabilization by adding two terms to the standard Galerkin formulation of the problem. The first term is the well-known SUPG (streamline-upwind Petrov–Galerkin) term. The second stabilization term is the PSPG (pressure-stabilizing/Petrov–Galerkin) term, which was introduced in [24, 25] to accommodate equal-order-interpolation velocity-pressure elements. In this work, the above analysis for the simulation of incompressible flows is extended to the simulation of flows driven by the combined action of buoyancy, surface tension and electromagnetic forces. This FEM fluid flow formulation is briefly addressed in the following discussion.

Let $\mathcal{E}$ denote the set of elements resulting from the finite element discretization of the computational domain Ω_l into subdomains Ω_l^e, $e = 1, 2, 3, ..., n_{el}$, where n_{el} is the number of elements. Associated with this discretization, we define the following finite element

interpolation and variational function spaces for the velocity and pressure:

$$S_v^h = \{v^h \mid v^h \in [H^{1h}(\Omega)]^{n_{sd}}, \ v^h \equiv \mathbf{0} \ on \ \Gamma_l - \Gamma_{tl}, \ v^h \cdot n = 0 \ on \ \Gamma_{tl}\} \quad (10)$$

$$V_v^h = \{w^h \mid w^h \in [H^{1h}(\Omega)]^{n_{sd}}, \ w^h \equiv \mathbf{0} \ on \ \Gamma_l - \Gamma_{tl}, \ w^h \cdot n = 0 \ on \ \Gamma_{tl}\} \quad (11)$$

$$S_p^h = V_p^h = \{q \mid q \in H^{1h}\} \quad (12)$$

Using standard notation [24, 25], we now write the stabilized Galerkin formulation of the flow equations as follows. Find $v^h \in S_v^h$ and $p^h \in S_p^h$ such that

$$\int_{\Omega_l} w^h \cdot \left(\frac{\partial v^h}{\partial t} + v^h \cdot \nabla v^h\right) d\Omega + \int_{\Omega_l} \epsilon(w^h) : \sigma(p^h, v^h) \, d\Omega + \int_{\Omega_l} q^h \nabla \cdot v^h \, d\Omega$$

$$+ \, Ra_T \, Pr \int_{\Omega_l} w^h \cdot \left(\theta^h - \frac{Ra_c}{Ra_T} c^h\right) e_g + Ha^2 Pr \int_{\Omega_l} w^h \cdot [\nabla \phi^h - v^h \times e_B] \times e_B \, d\Omega$$

$$+ \sum_{e=1}^{n_{el}} \int_{\Omega_l^e} (\delta^h + \epsilon^h) \cdot \left(\frac{\partial v^h}{\partial t} + v^h \cdot \nabla v^h - \nabla \cdot \sigma(p^h, v^h) + Pr \, Ra_T \theta^h e_g - Pr \, Ra_c c^h e_g\right)$$

$$+ \, Ha^2 Pr[\nabla \phi^h - v^h \times e_B] \times e_B) d\Omega - \int_{\Gamma_{tl}} w^h \cdot (\sigma^h \cdot n) \, d\Gamma = 0,$$

$$\forall w^h \in V_v^h, \quad \forall q^h \in V_p^h. \quad (13)$$

In the above formulation, two stabilizing terms have been added to the standard Galerkin formulation; the one with δ^h is the SUPG term and the one with ϵ^h is the PSPG term. More details on the form of these stabilizing terms can be obtained from [24, 25]. The above fluid flow formulation for coupled buoyancy, surface tension, and electromagnetically driven flows is combined with an SUPG formulation for the heat and solute transport equations with discontinuous weighting functions and a classical Galerkin formulation for the electric potential equation.

After spatial discretization of the variational forms of the governing equations, the following system of nonlinear ordinary differential equations is obtained for the solution of the velocity field v, the pressure p, the temperature field θ, and the electric potential field ϕ in the liquid domain:

$$[\hat{\mathbf{M}} + \hat{\mathbf{M}}_\delta]\{\dot{\theta}\} + [\hat{\mathbf{N}}(v) + \hat{\mathbf{N}}_\delta(v)]\{\theta\} + [\hat{\mathbf{K}} + \hat{\mathbf{K}}_\delta]\{\theta\} = \{\hat{\mathbf{F}}\} \quad (14)$$

$$[\mathbf{M} + \mathbf{M}_\delta]\{\dot{v}\} + [\mathbf{N}(v) + \mathbf{N}_\delta(v)]\{v\} + [\mathbf{K} + \mathbf{K}_\delta]\{v\} - [\mathbf{G} + \mathbf{G}_\delta]\{p\} + [\mathbf{D} + \mathbf{D}_\delta]\{v\}$$

$$+ [\mathbf{B} + \mathbf{B}_\delta]\left\{\theta - \frac{Ra_c}{Ra_T}c\right\} + [\mathbf{H} + \mathbf{H}_\delta]\{\phi\} + [\mathbf{S}]\{\theta\} = \mathbf{F} + \mathbf{F}_\delta \quad (15)$$

$$\mathbf{G}^T\{v\} + \mathbf{M}_\epsilon\{\dot{v}\} + \mathbf{N}_\epsilon(v)\{v\} + \mathbf{K}_\epsilon\{v\} + \mathbf{G}_\epsilon\{p\} + \mathbf{D}_\epsilon\{v\}$$

$$+ \mathbf{B}_\epsilon\left\{\theta - \frac{Ra_c}{Ra_T}c\right\} + \mathbf{H}_\epsilon\{\phi\} = \mathbf{E} + \mathbf{E}_\delta \quad (16)$$

$$[\tilde{\mathbf{K}}]\{\phi\} = [\tilde{\mathbf{P}}]\{v\}. \quad (17)$$

In the above equations, $\{v\}$ denotes the vector of nodal values of the velocity field v, $\{\dot{v}\}$ the time derivative of $\{v\}$, $\{p\}$ the vector of nodal values of the pressure field p, $\{\theta\}$ the vector of nodal values of the temperature field θ, $\{\dot{\theta}\}$ the time derivative of $\{\theta\}$, and $\{\phi\}$

the vector of nodal values of the electric potential field ϕ. The matrices $\mathbf{M}$, $\mathbf{N}(\mathbf{v})$, $\mathbf{K}$, and $\mathbf{G}$ (Eqs. (15) and (16)) are derived, respectively, from the time-dependent, advective, viscous, and pressure terms. The matrix $\mathbf{B}$ in these equations is derived from the buoyancy term, whereas the matrices $\mathbf{D}$ and $\mathbf{H}$ are derived from the electromagnetic contributions. The matrix $\mathbf{S}$ is obtained from the surface-tension term. The subscripts δ and ϵ are used here to identify the SUPG and PSPG contributions, respectively. Similar notation is used for the discrete heat equation in the melt (Eq. (14)). The discrete equations for the solute transport equation in the melt and heat transport in the solid are similar in form to the discrete melt temperature equation shown in Eq. (14).

A moving finite element methodology is used together with an energy preserving weak form of the Stefan condition to allow tracking of the interface Γ_I [26]. The extra convection terms resulting from the mesh motion are implicitly incorporated into the nonlinear matrices $\hat{\mathbf{N}}$, $\hat{\mathbf{N}}_\delta$, $\mathbf{N}$, $\mathbf{N}_\delta$, and $\mathbf{N}_\epsilon$ in the discrete forms of the transport Eqs. (14)–(16).

The time integration of the heat and solute transport equations is achieved using a predictor–corrector scheme [26]. A one-step generalized trapezoidal rule (T1 formulation of [24]) is used for the time integration of the flow equations. The electric potential equation yields the linear system of Eq. (17), which is solved by a standard procedure. Although the discrete equations for the various transport problems are coupled, the solution of these equations at each time step is achieved in a decoupled fashion. The finite element grids of the solid and liquid domains are first updated using the calculated front velocity at the earlier time step. The solution of the heat and solute transport equations in the melt are obtained next, which is followed by the solution of the flow equations. This is followed by the solution of the electric potential equation. Next, the heat transport problem in the solid domain is solved. Finally, the weak form of the Stefan condition is solved to obtain the interface velocity field, which is used to update the finite element grids to the next time step. This solution technique has proven to be accurate and computationally efficient for the various numerical example problems tested.

Mass lumping and preconditioning were employed here to improve the efficiency of the method and to ensure smooth solutions. At each time step of the flow equations, a system of linear equations $\mathbf{A}\mathbf{x} = \mathbf{b}$ needs to be solved. In evolution problems, such as the one under consideration, the stiffness matrix $\mathbf{A}$ evolves very slowly. Thus, the stiffness matrix $\tilde{\mathbf{A}}$ calculated a few time steps earlier can be considered as a close approximation to the current stiffness matrix $\mathbf{A}$, and hence can be employed as a very good preconditioner. Using this idea as the basis, an LU-factorization of the stiffness matrix $\tilde{\mathbf{A}}$ is calculated at regular time steps and is employed as a preconditioner in solving the flow equations. The period after which the LU-factorization is performed is a compromise between the computational cost and the improvement in the condition number $\kappa(A)$ of the resulting system. A preconditioned stabilized bi-conjugate gradients method (BICGSTAB) [36] for the solution of nonsymmetric system of linear equations is used for the solution of the resulting linear system at each time step. Further details on this preconditioning algorithm are available in a recent technical report [37], wherein validation and computational performance studies are presented for several benchmark incompressible flow problems using this solution technique. In addition to confirming the accuracy of the solution procedures, the reported studies demonstrated the effectiveness of the preconditioning algorithm in reducing the CPU costs by a factor as high as 20 [37].

The entire implementation of the various transport equations was achieved using an object-oriented framework [26]. In addition to the validation studies reported above, the

moving FEM formulation and numerical solution procedures have been successfully verified through comparisons (e.g., calculated temperature, flow fields, and the solid–liquid interface positions at various times) with reported numerical results for the solidification of a pure substance [13]. The numerical accuracy has also been confirmed through extensive comparisons with existing numerical results obtained using finite differences techniques for coupled thermocapillary and buoyant flow in a rectangular cavity [2, 10, 21]. The additional effects of an externally applied magnetic field have also been studied and compared with the results reported in [21]. The obtained computational results were very satisfactory and confirmed the accuracy of the developed solution procedures.

In the example problems reported in this paper, for all subproblems except the flow equations, a stopping tolerance of $1.0E-06$ was used to terminate the solution of the nonlinear equations. The solution of the flow equations was stopped after two passes per time step, as suggested in [24]. Computations were carried out on a IBM RS6000 work station. The overall cost of solving the various transport equations per time step was about 9 CPU seconds. The entire computations spanned over 40,000 time steps.

4. SOLIDIFICATION OF ANTIMONY-DOPED GERMANIUM IN AN OPEN-BOAT CONFIGURATION

4.1. A Reference Binary Alloy Solidification Problem

A rectangular cavity is considered with an open free surface of dimensions 2 cm×1 cm initially filled with molten antimony-doped germanium at 40°C overheat. The right-hand side vertical mold wall Γ_{ol} is maintained at the initial temperature, whereas the left vertical mold wall Γ_{os} is suddenly cooled to a temperature 40°C below the melting temperature of pure germanium and maintained at that temperature for $t > 0$. The solidification process starts and takes place under standard laboratory conditions (normal gravity, no magnetic field). The thermophysical properties were compiled from References [16] and [38] and are listed in Table I. It is assumed that the small concentrations of antimony do not lead to solutal-driven convection. Similar assumptions were employed in [38] for the growth of dilute gallium-doped germanium. The dimensionless parameters are summarized in Table II.

TABLE I
Thermophysical Properties of Germanium

Thermal conductivity of the melt	K_l (W/°Ccm)	0.39
Thermal conductivity of the solid	K_s (W/°Ccm)	0.17
Density of the melt	ρ_l (g/cm^3)	5.5
Density of the solid	ρ_s (g/cm^3)	5.5
Specific heat of the melt	$C_{p,l}$ (J/°C · g)	0.39
Specific heat of the solid	$C_{p,s}$ (J/°C · g)	0.39
Melting temperature	T_m (°C)	937.4
Kinematic viscosity	ν (cm^2/s)	0.0013
Heat of solidification	L_H (J/g)	460
Surface tension coefficient	$d\sigma/dT$ (N/mK)	-0.26×10^{-4}
Thermal expansion coefficient	β_T (°C^{-1})	5.0×10^{-4}
Mass diffusivity of dopant	D (cm^2/s)	5.5×10^{-4}
Equilibrium partition coefficient	κ	0.003

TABLE II

**Dimensionless Groups and Their Characteristic Values
for Modeling Antimony-Doped Germanium Growth in an
Open-Boat Configuration**

Prandtl number	Pr	0.007
Thermal Rayleigh number	Ra_T	82931
Solutal Rayleigh number	Ra_c	0.0
Lewis number	Le	330.0
Marangoni number	Ma	-8×10^3
Hartmann number	Ha	0.0–400.0
Stefan number	Ste	0.034
Heat conductivity ratio	R_k	0.4358
Heat diffusivity ratio	R_α	0.4358
Slope of the liquidus	m	≈ 0

In problems dealing with surface-tension-driven flows, grid selection is influenced by the strength of the fluid flow near the free surface and, in particular, by the large velocity and temperature gradients characteristic of the singular region in the cold corner. For Marangoni numbers associated with most flows, an extremely fine grid is required to resolve the fine details of the corner flow precisely [14]. Moreover, in the transient solidification of a binary mixture, this problem is aggravated because of the presence of the moving solid–liquid interface. Hence, the finite element mesh was biased toward the free surface in order to capture the essential details of the wall shear layers. The finite element grid consisted of 3200 bilinear elements and 3321 nodes and is shown in Fig. 2. Through several computational tests with various grid sizes, it was determined that the above discretization was sufficient to capture the macroscopic aspects of the fluid flow, solute, and temperature patterns that are the main focus of this work. Figure 2 also provides the imposed boundary conditions used in the various simulations.

Because of the fact that the time scale associated with cell formation is much less than that associated with the solidification process and because of the presence of large velocity
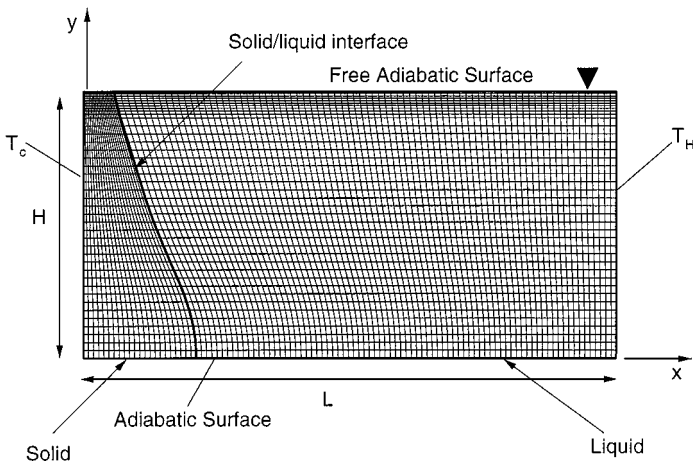

FIG. 2. Sample finite element mesh at time $\tau = 10$ for the solid and liquid domains.

gradients near the free surface, it was necessary to use small time steps in the calculation ($\Delta\tau = 2.5 \times 10^{-4}$). The simulations were terminated at $\tau = 10$ when the flow field had almost achieved a steady state pattern.

The simulation shows that at early times the thermal gradients in the originally quiescent melt cause surface-tension gradients on the free surface and density gradients in the bulk liquid. This leads to combined buoyancy and thermocapillary convection in the fluid. The fluid velocities are maximum at the top free surface in regions close to the interface Γ_I. Continuity of the fluid flow slowly leads to counter-clockwise circulation of the melt filling the entire cavity. As the solidification process proceeds further, the interface Γ_I starts to curve, with more solid volume formed at the bottom compared to the top part of the cavity. At around $\tau = 1$, two distinct weak recirculating cells form near the hot end of the cavity ($1.7 < x < 2.0$), in addition to the main (strong) counter-clockwise recirculating cell filling most of the cavity. With continued solidification, the cells slowly merge forming a variety of weak cell patterns near the hot end. The main recirculating cell maintains its flow pattern, however, slowly increasing the strength of the circulation. Figure 3 shows the streamlines, isopleths (iso-composition lines) and isotherms at intermediate times $\tau = 2$ and $\tau = 5$, whereas Fig. 4 shows the corresponding fields at the final time $\tau = 10$. Note the significant
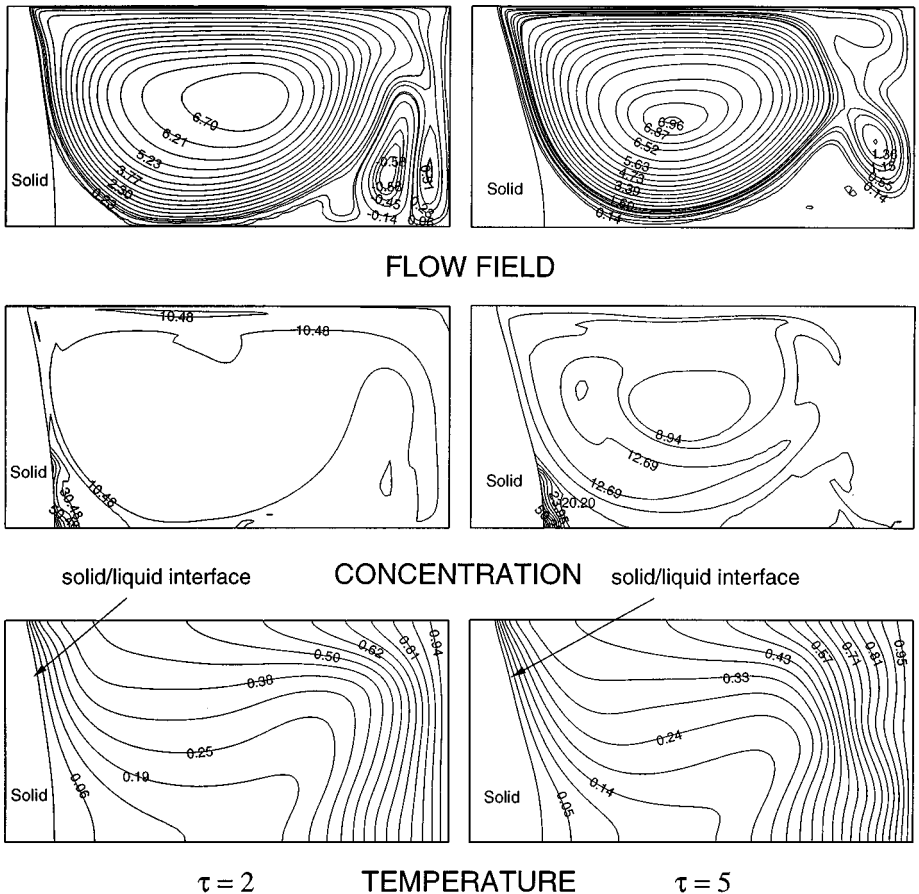

FIG. 3. Calculated contours of stream function, solute concentration, and temperature fields at times $\tau = 2$ and $\tau = 5$ for the solidification of SbGe under normal gravity conditions and zero magnetic field.
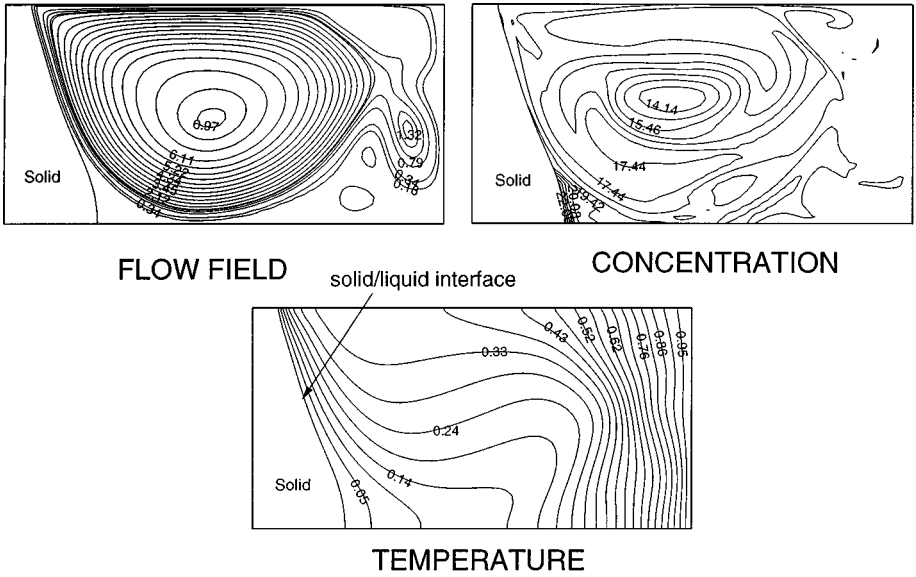
FIG. 4. Calculated contours of stream function, solute concentration, and temperature fields at times $\tau = 10$ for the solidification of SbGe under normal gravity conditions and zero magnetic field.

evolution in the flow structure as time progresses. Also, one can easily note that the weak circulating cell patterns at the right end have a marked effect on the shape of the isotherms (note the wavy nature of the isotherms) near the hot end of the cavity. Finally, it is to be emphasized that the significant variation in the dopant distribution as well as the prominent curvature of Γ_I can be attributed mainly to the strong convection (coupled buoyancy and thermocapillary flow) in the bulk liquid. The prominent distortion of Γ_I near the free surface is mainly the result of the high velocity gradients induced by the thermocapillary effect. This strong flow significantly retards the local solidification velocities in the upper part of the cavity.

Figure 5 presents the history of the concentration on Γ_I during the entire simulation. Since the interface concentration is directly proportional to the solid concentration ($C_s = \kappa C_l$),
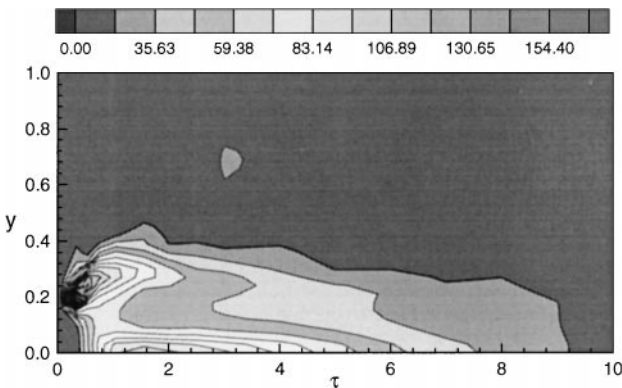

FIG. 5. Calculated history of the solid–liquid interface concentration during the entire simulation of SbGe solidification under normal gravity and zero magnetic field conditions.
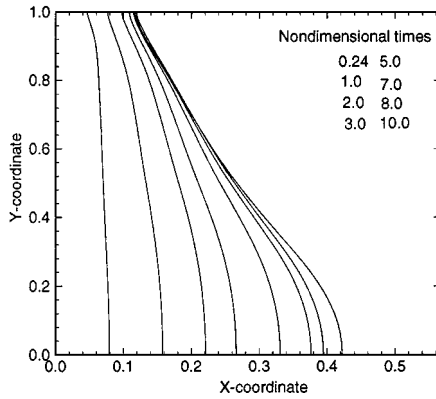
FIG. 6. Predicted solid–liquid interface location at intermediate times for the simulation of SbGe solidification under normal gravity and no magnetic field.

this plot effectively shows the pattern of the solute variation obtained in the final solid. As can be clearly seen, the intricate fluid flow pattern appears to have a profound effect on the obtained macroscopic solute distribution. Initially the heavy solute descends along the interface Γ_I and settles at the bottom of the cavity. This steady accumulation of solute at the base continues as more solid is formed. Simultaneously, the convection in the melt becomes stronger, and this strong convection transports and redistributes the rejected solute throughout the entire cavity. This vigorous solute convection leads to macroscopic variation of the rejected solute, as shown in Fig. 5, and consequent inhomogeneity in the final solid.

The fluid flow in the melt also has significant influence on the shape of Γ_I. Figure 6 shows the calculated shapes Γ_I at various times. Note that, at early times, Γ_I is almost vertical except very near the free surface. At later times, the macroscopic curvature of Γ_I becomes more prominent because of the steadily increasing strength and size of the main counter-clockwise recirculating cell.

4.2. *Effects of Reduced Gravity on the Solidification Problem*

For several years there has been the opportunity to grow crystals under conditions of reduced gravity in space missions and ballistic rocket flights. The main reason for doing this is to obtain nearly pure diffusive transport conditions in the fluid nutrient. However, this is only guaranteed if not only buoyancy but also Marangoni convection is avoided. As will be shown here, under reduced gravity conditions thermocapillary convection is a dominant forcing agent that has significant influence on various solidification parameters.

To assess the relative importance of thermocapillary versus buoyancy effects on solidification, a complete calculation was performed for solidification in a very low-gravity $(g = 10^{-5} g_{earth})$ environment. This configuration corresponds to a case of almost pure thermocapillary flow. Figures 7 and 8 show the temperature, concentration, and flow fields at a few intermediate times for the above solidification problem.

At early times ($\tau < 0.5$), thermal gradients on the free surface lead to surface-tension gradients and a thermocapillary flow develops slowly, forming a small counter-clockwise cell around the free surface very close to Γ_I. There is almost no convection in the lower part of the cavity at this time. As the solidification proceeds further, the strength of this recirculating fluid flow slowly increases, along with a steady increase in the size of the cell.
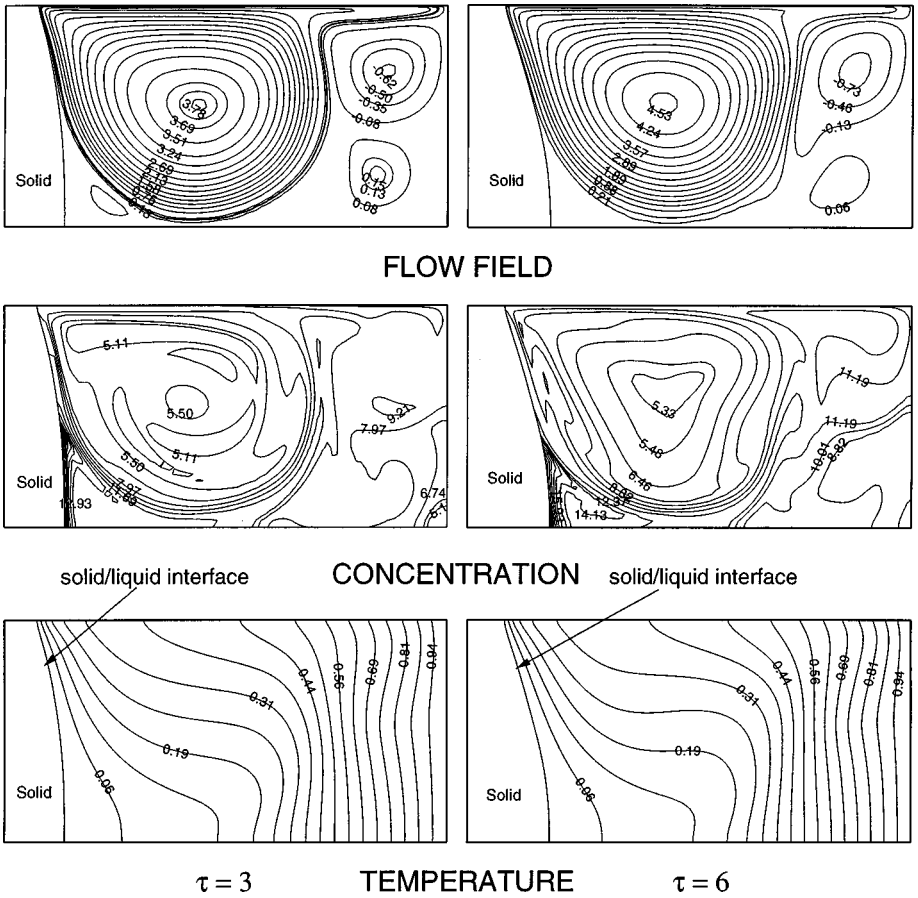
FIG. 7. Calculated contours of stream function, solute concentration, and temperature fields at times $\tau = 3$ and $\tau = 6$ for the solidification of SbGe under reduced gravity ($g = 10^{-5} g_{earth}$) conditions and zero magnetic field.

Around $\tau = 2$, the main recirculating cell fills almost the entire cavity. At the same time, a secondary cell pattern forms at the right end of the cavity. After around $\tau = 3$, there is almost no change in the structure of the main cell, even though its strength steadily increases with time (see Figs. 7 and 8).

This complex evolution of the melt flow has significant impact on various solidification parameters. Figure 9 presents the history of the concentration on Γ_I during the entire solidification simulation. Note the significant difference between the solute pattern obtained under normal and reduced gravity conditions (compare Figs. 5 and 9). The reason for this difference lies in the distinct difference in the evolution of the melt flow in the two cases. In the present case of almost pure thermocapillary flow, convection in the bulk liquid initiates at the top free surface and slowly propagates inward. This means that at very early times the rejected solute at Γ_I slowly collects near the free surface and forms a high solute concentration region in the upper left corner of the liquid domain. This region slowly moves downward into the liquid as the solidification progresses further. This explains the steady movement of the "high concentration spots" in Fig. 9 from the top to the bottom as time increases. In fact, there is a direct correlation between the size and center
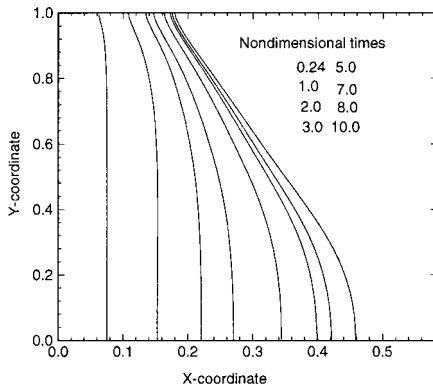
FIG. 8. Calculated contours of stream function, solute concentration, and temperature fields at time $\tau = 10$ for the solidification of SbGe under reduced gravity ($g = 10^{-5} g_{earth}$) conditions and zero magnetic field. Notice the significant influence of the flow field on the solute distribution in the melt.

of the main counter-clockwise circulation cell and the height at which the solute "high concentration spots" are formed. At around $\tau = 0.5$, the center of the circulation is close to $y \approx 0.8$ which is about the same height at which the first concentration spot is observed in Fig. 9. With continued solidification, this cell increases in size, and the center of the circulation moves downward. This is consistent with the movement of the "high concentration spots" lower down along the y-axis in Fig. 9. By around $\tau \sim 2.5$, the main cell has occupied almost the entire cavity, and the center of the recirculating cell is at $y \approx 0.5$, which is again consistent with the height at which the last "high concentration spot" is observed. This flow pattern of the main recirculating cell is maintained throughout the rest of the simulation, which is in agreement with the solute pattern seen in Fig. 9 for times $\tau > 3.0$.

FIG. 9. Calculated history of the solid–liquid interface concentration during the entire simulation of SbGe solidification under reduced gravity ($g = 10^{-5} g_{earth}$) conditions and zero magnetic field.

FIG. 10. Predicted solid–liquid interface location at intermediate times for the simulation of SbGe solidification under reduced gravity ($g = 10^{-5} g_{earth}$) conditions and no magnetic field.

It is quite obvious from Fig. 9 that thermocapillary melt flow plays a significant part in the type and scale of solidification microstructures obtained, especially under reduced gravity conditions. The complex fluid flow in the melt also has significant influence on the shape of Γ_I. Figure 10 shows the calculated solid–liquid interface locations at various times. It is quite intriguing to note that even in the absence of buoyancy-driven convection, the distortion of the otherwise flat Γ_I is quite prominent. This clearly demonstrates the role that thermocapillary convection plays on the dynamics of the solidification process.

In order to further investigate the relative influence of buoyancy-driven convection and thermocapillary convection on the dynamics of the transient solidification process, an extensive series of simulations were conducted under various levels of gravity. As before, there is no imposed magnetic field. Figure 11 depicts the variety of flow patterns at time
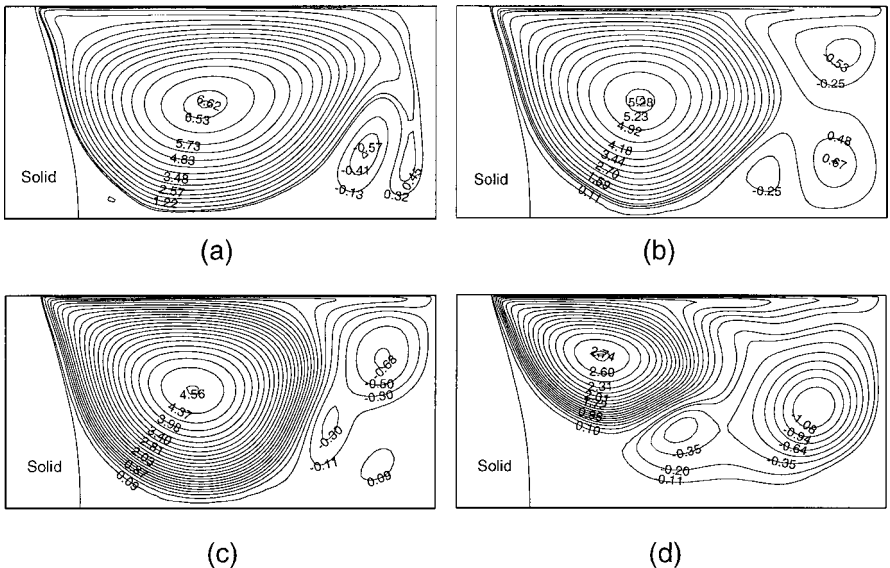

FIG. 11. Calculated contours of stream function at time $\tau = 5$ for the solidification of SbGe under varying levels of gravity: (a) $0.5 g_{earth}$, (b) $0.1 g_{earth}$, (c) $0.01 g_{earth}$, and (d) $10^{-5} g_{earth}$. There is no imposed magnetic field. Notice the significant change in the structure of the flow with decreasing gravity.

$\tau = 5$ obtained for varying levels of gravity. As can be seen from this figure, decreasing the magnitude of gravity significantly alters the flow pattern. Altering the strength of gravity varies the relative influence of buoyancy and thermocapillary convection on the solidification process. This is characterized by the dimensionless Bond number, defined as the ratio of buoyancy to surface tension forces ($Bo \equiv Ra_T / Ma$). At normal gravity levels the Bond number is of the order 10 (in the present example), and hence buoyancy effects dominate over the surface-tension effects (even though the latter have a significant influence on the solidification phenomena). However, at very low values of gravity (see Fig. 11d), the Bond number is close to zero. In this case the fluid flow is driven primarily by the surface-tension gradients on the free surface. This explains the significant change in the flow pattern observed in the two extreme cases. As one should expect, for intermediate gravity levels (see Figs. 11a–11c), the combined action of buoyancy and surface-tension forces reveals a rich variety of different flow structures depending on the magnitude of the Bond number. Finally, it is to be noted that there is a steady decrease in the strength of the flow with decrease in the magnitude of the gravity vector. This is easily understood by considering the fact that, while surface tension forces remain unaltered, the magnitude of the buoyancy force steadily decreases with gravity.

4.3. *Effects of an Externally Applied Magnetic Field*

In recent years, strong magnetic fields have been used in crystal growth of semiconductor materials in order to reduce macroscopic inhomogeneity in the crystal by suppression of buoyancy driven convection (see Chapter 4 in [17]). In addition, static magnetic fields have also been used to avoid occurrence of unsteady convection which is considered to be the origin of micro-inhomogeneity in crystals (see Chapter 7 in [17]). It is becoming increasingly evident that the homogeneity of crystals can be drastically influenced by imposed magnetic fields. Furthermore, recent studies indicate that there is tremendous potential in effectively using magnetic fields in order to control the solidification process [39]. In an attempt to explore this effect numerically, we consider the influence of an externally applied magnetic field on the above solidification problem.

It is well known that application of a magnetic field damps the melt flow. Kim *et al.* [20] clearly demonstrated through an asymptotic analysis that the intensity of the flow in the liquid melt varies as Ha^{-2}. Considering this fact and the magnitude of the Rayleigh number in the current example problem, the effect of a horizontal magnetic field of strength corresponding to $Ha = 100$ is first considered. This value of Hartmann number is such that the flow is affected significantly by the applied magnetic field, but is also such that the melt flow is not completely damped and interesting interactions of buoyancy-, thermocapillary-, and electromagnetically-driven flow can be studied.

Results obtained for solidification under normal gravity conditions and a horizontal magnetic field ($Ha = 100$) are shown in Figs. 12 and 13. As can be clearly seen by comparing the flow fields in Figs. 3 and 4 and Figs. 12 and 13, as expected the application of a sufficiently strong magnetic field significantly damps the melt convection in the solidifying melt. Furthermore, one can note from Figs. 12 and 13 that fluid velocities in the vertical direction are damped in the entire liquid domain. This fluid behavior can be easily understood from the fact that maximum electromagnetic damping of the fluid occurs when the velocity field v is oriented orthogonal to the unit magnetic field vector e_B because of the particular form of the electromagnetic damping force ($\mathbf{F} \propto (v \times e_B) \times e_B$).
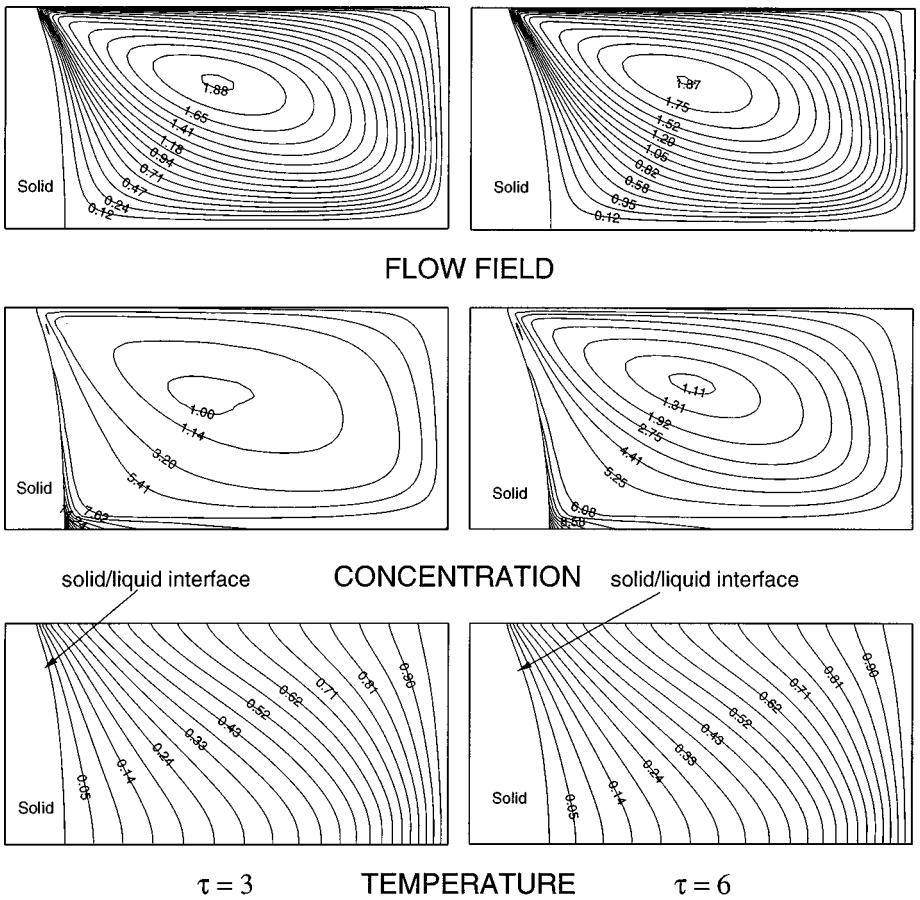
FIG. 12. Calculated contours of stream function, solute concentration, and temperature fields at times $\tau = 3$ and $\tau = 6$ for the solidification of SbGe under normal gravity conditions and a horizontally imposed external magnetic field ($Ha = 100$).

In the above results corresponding to solidification under normal gravity conditions, the Bond number is approximately 10 and hence buoyancy dominates over surface tension forces. In order to study the influence of a externally applied magnetic field on a solidification problem driven mainly by surface tension forces, a similar simulation corresponding to almost zero gravity was performed. Results of the calculation are illustrated in Figs. 14 and 15.

As can be seen from Figs. 14 and 15, the simulation under reduced gravity conditions demonstrates that application of a magnetic field plays an entirely different role in the absence of gravity. Since the gravity level is extremely low ($g = 10^{-5} g_{earth}$), the main driving force for convection in the fluid is thermocapillary convection. Thermal gradients on the free surface lead to a surface-tension-driven flow. Continuity leads to a "back flow." Since the magnetic field is oriented in the horizontal direction, velocity components in the vertical direction are significantly damped. Hence, the fluid circulation tends to be as "flat" as possible. This leads to the counter-clockwise recirculating flow structure shown in Fig. 14. Note that the strong fluid flow is restricted mainly to the upper part of the cavity. Immediately below this counter-clockwise circulation, a shear-driven clockwise weak circulation as well as a counter-clockwise weak circulation resulting from buoyancy can also be observed. This
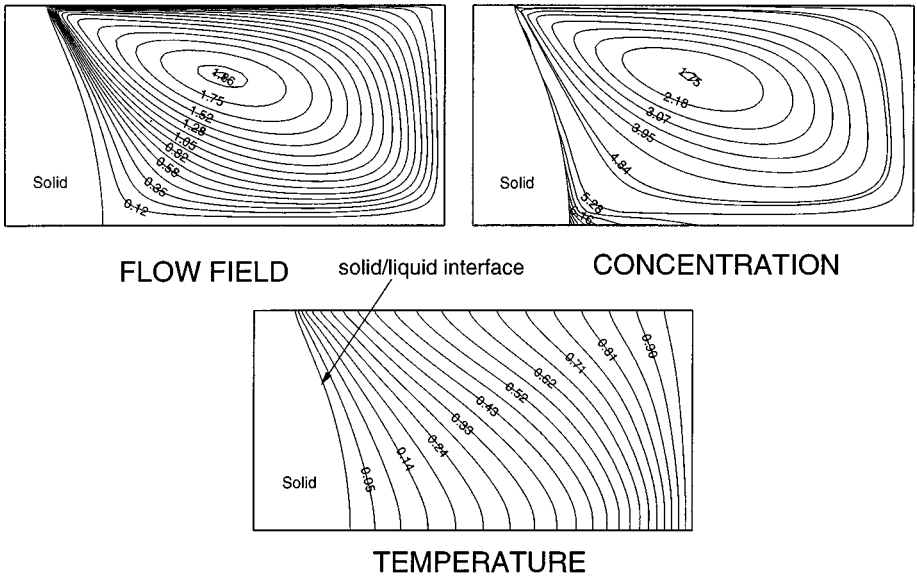
FIG. 13. Calculated contours of stream function, solute concentration, and temperature fields at time $\tau = 10$ for the solidification of SbGe under normal gravity conditions and a horizontally imposed external magnetic field ($Ha = 100$).

fluid flow structure is maintained throughout the entire solidification process, although the intensity of the convection keeps varying with time.

This peculiar behavior of the fluid flow in the melt has important consequences on the solidification problem. As illustrated in Figs. 14 and 15, the temperature contours are almost vertical except very near the free surface. The distortion of the isotherms near the free surface is a direct consequence of the melt flow in that region. The solute concentration field is also affected by the complex fluid flow. At very early times, because of the absence of convection, the solute rejected at the interface Γ_I is transported into the bulk liquid mainly via diffusion. Because of the high Lewis number ($Le = 330$) of the system, this diffusion layer is restricted mainly to a region close to Γ_I. With continued solidification, the melt flow develops, and the solute is carried by the convecting fluid. Since the fluid flow is such that the strong melt flow is mainly restricted to the upper part of the cavity, the solute transport by convection is also confined mainly to this region of the cavity. The solute transport in the bottom parts of the cavity is mainly through diffusion and the weak shear- and buoyancy-driven cells. This explains the solute patterns seen in Fig. 14 corresponding to time $\tau = 2$. With further solidification, some of the solute collected in the upper regions of the cavity is slowly transported to the bottom part as a result of the combined effects of buoyancy and shear driven convecting weak flow as well as through diffusion. Because of the weak nature of the shear- and buoyancy-driven cells, the solute collects at the bottom and forms the stratified layer, as seen in Figs. 14 and 15 at later times.

Figure 16 compares the solid–liquid interface solute pattern for the above two simulations (under normal and reduced gravity conditions) with an applied magnetic field. As expected, markedly different transport patterns in the two systems lead to entirely different form of solute segregation. As seen in Fig. 16(a), the maximum solute concentration under normal gravity conditions is seen in the bottom part of the rectangular cavity at very early times.
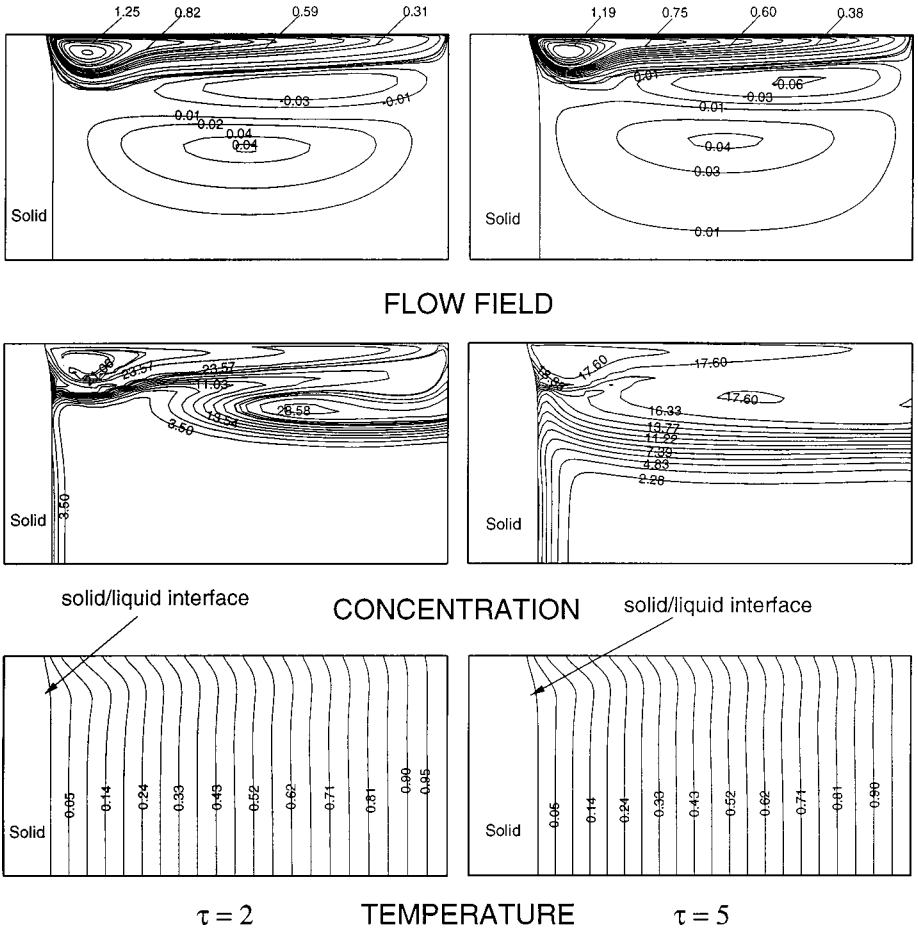
FIG. 14. Calculated contours of stream function, solute concentration, and temperature fields at times $\tau = 2$ and $\tau = 5$ for the solidification of SbGe under reduced gravity ($g = 10^{-5} g_{earth}$) conditions and a horizontally imposed external magnetic field ($Ha = 100$).

This is consistent with the transport patterns seen in Figs. 12 and 13. In contrast, Fig. 16b shows that the maximum solute collection occurs very near the free surface and at early times. This trend is in conformity with the fluid flow circulation seen in Figs. 14 and 15, which is restricted mainly to regions close to the free surface.

Distinct transport behavior of the two systems under different gravity conditions also has important implications on the shape of Γ_I. As can be clearly seen by comparing Figs. 12 and 13 and Figs. 14 and 15, the interface macroscopic curvature is predominantly decreased under reduced gravity conditions. In order to quantify and compare the extent of distortion of Γ_I during the two simulations, a standard deviation σ_s is defined as

$$\sigma_s(t) = \left\{ \frac{1}{N} \sum_{i=1}^{N} [s(i, t) - \bar{s}(t)]^2 \right\}^{\frac{1}{2}}, \tag{18}$$

where $s(i, t)$ is the nodal location of the ith interface node, and $\bar{s}(t)$ is the average of all the interface nodal locations at time t. Figure 17 compares this standard deviation for the
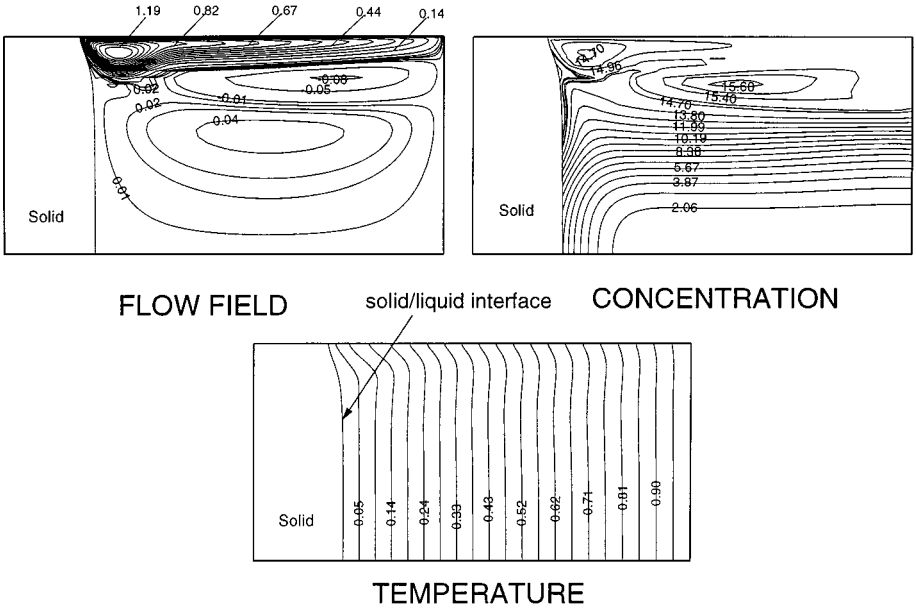
FIG. 15. Calculated contours of stream function, solute concentration, and temperature fields at time $\tau = 10$ for the solidification of SbGe under reduced gravity ($g = 10^{-5}g_{earth}$) conditions and a horizontally imposed external magnetic field ($Ha= 100$).

above simulations. As can be seen from this figure, the maximum interface distortion for the reduced gravity case is around four times less than that corresponding to the case under normal gravity conditions. Note that this marked difference in the interface macroscopic curvature is not evident without the presence of a magnetic field (compare the shapes of Γ_I in Figs. 6 and 10). Also note that the steady increase in the curvature of Γ_I in Fig. 17 is a direct consequence of the increasing strength of the fluid flow in the melt with time.

4.3.1. Effects of varying the strength of the applied magnetic field. It is quite evident from the analysis presented earlier that an applied magnetic field plays a very important role in the solidification process. In an attempt to shed further light on the various interesting phenomena, a sequence of simulations was performed under varying magnetic field strengths.
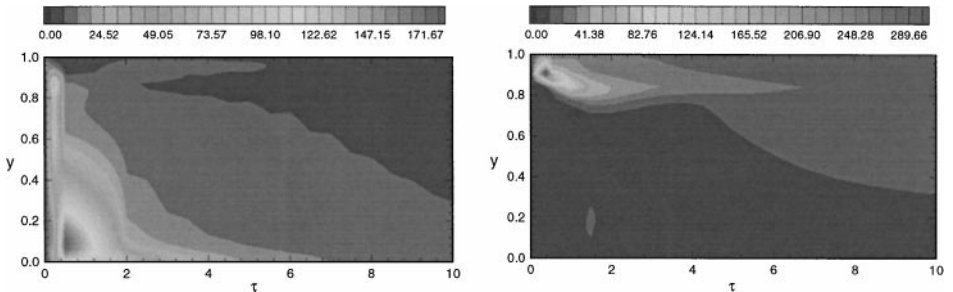

FIG. 16. Calculated history of the solid–liquid interface concentration during the entire simulation of SbGe solidification under the influence of a horizontally applied magnetic field ($Ha = 100$): (a) normal gravity conditions and (b) reduced gravity ($g = 10^{-5}g_{earth}$) conditions.
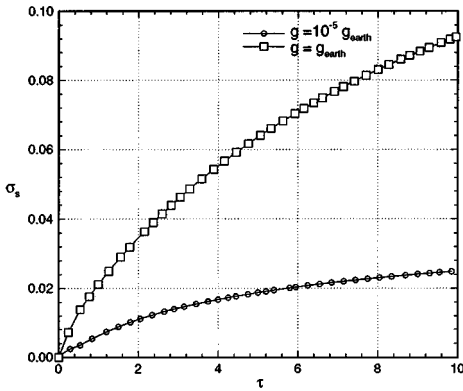
FIG. 17. The variation of the standard deviation $\sigma_s(t)$ for the solidification simulation under normal and reduced gravity ($g = 10^{-5} g_{earth}$) conditions. There is an imposed magnetic field ($Ha = 100$) in the horizontal direction. Note the significant drop in the interface macroscopic curvature under reduced gravity conditions.

Simulations were performed under magnetic field strengths in the range $0 < Ha < 400$ applied in the horizontal direction. Calculations were performed both under normal and under extremely low gravity levels. Such a study would help us understand the effects of magnetic fields on the two extreme cases considered earlier—one solidification problem driven mainly by buoyancy forces and another driven mainly by surface tension forces on the free surface.

Figure 18 illustrates the variety of melt flow patterns obtained by varying the strength of the applied magnetic field. The results correspond to time $\tau = 10$. Figures 18a–18d depict the flow patterns corresponding to solidification under normal gravity conditions, whereas Figs. 18e–18h show the flow fields for the simulation under reduced gravity conditions. In both cases, the predominant effect of increasing the magnetic field is to damp the fluid flow. This is very clear by comparing the maximum stream function values at various magnetic field strengths (see Fig. 19). In the simulation case under normal gravity conditions, increasing the magnetic field strength also significantly changes the melt flow pattern. When a sufficiently strong magnetic field is applied ($Ha > 25$), secondary cell formation is suppressed, and the central circulation is seen to spread gradually over the whole cavity. On a further increase in the Hartmann number ($Ha \approx 100$), the streamlines accumulate near the free surface and the interface Γ_I indicating the existence of strong boundary layers on these boundaries. Increasing the magnetic field strength further reveals a very interesting fluid behavior. As seen in Fig. 18d, an entirely different flow structure evolves when the Hartmann number is increased to a value of 200. The flow pattern shows that a strong surface-tension-driven counter-clockwise cell forms very near the free surface, whereas a weak buoyancy-driven recirculating cell occupies the rest of the cavity. This separation of the convection rolls of the thermocapillary convection and of buoyant convection is triggered by the suppression of vertical velocities because of the high magnetic field. Since the applied horizontal magnetic field damps vertical velocities but has no effect on horizontal components, the thermocapillary "back flow" occurs very close to the free surface.

In contrast to the normal gravity case, the simulations under reduced gravity conditions show a more gradual change in the flow structure. Since the flow is mainly driven by surface-tension forces, buoyancy plays almost no role in these simulations. At low Hartmann numbers ($Ha < 20$), the thermocapillary flow develops sufficient intensity such that the
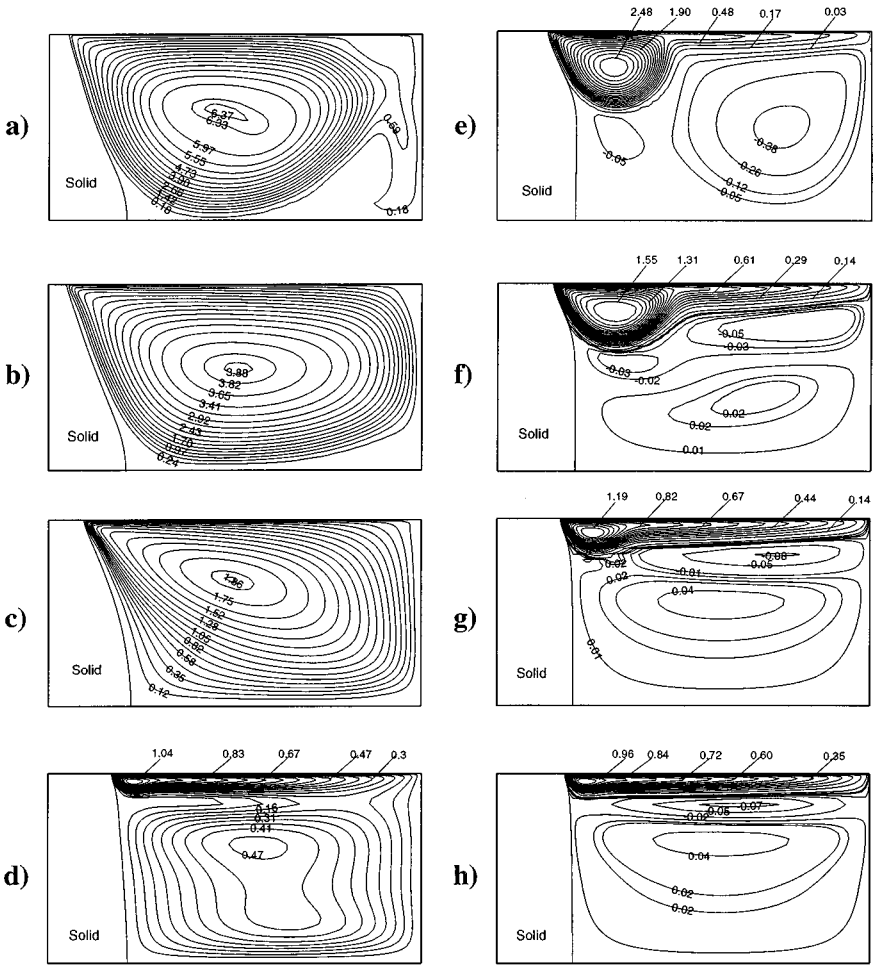
FIG. 18. Calculated contours of stream function at time $\tau = 10$ for the solidification of SbGe under the influence of an externally imposed horizontal magnetic field. Solidification under normal gravity conditions: (a) $Ha = 10$; (b) $Ha = 50$; (c) $Ha = 100$; (d) $Ha = 200$. Growth under reduced gravity ($g = 10^{-5} g_{earth}$) conditions: (e) $Ha = 10$; (f) $Ha = 50$; (g) $Ha = 100$; (h) $Ha = 200$.

recirculating cell pattern occupies almost the entire upper half of the melt domain. However, with increasing values of the Hartmann number, the magnetic field significantly damps the vertical fluid motion and restricts the propagation of the surface-tension-driven fluid flow into the inner parts of the cavity. Hence, at large Hartmann numbers ($Ha > 100$), the thermocapillary flow is restricted mainly to a layer adjacent to the free liquid surface (see Fig. 18(h)).

The significant variation in the various transport phenomena with varying magnetic field strengths has a tremendous impact on the solidification parameters such as the shape of the interface Γ_I. For example, as can be deciphered by comparing Fig. 18a and Fig. 18d, increasing the magnetic field strength increases the solidification velocities on the top surface. Furthermore, the overall interface shapes are also affected significantly. Similar behavior is observed even for solidification under reduced gravity conditions, though the change in solidification growth velocities is not as prominent. As one can note from
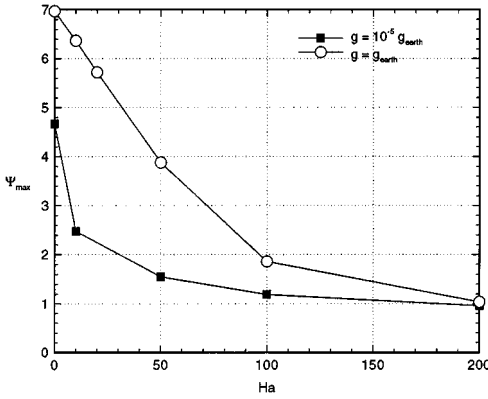
FIG. 19. Maximum value of stream function as a function of the applied Hartmann number for solidification simulations under normal as well as extremely low gravity levels ($g = 10^{-5} g_{earth}$). The applied magnetic field is aligned along the positive x-direction.

Fig. 18h, solidification under reduced gravity and sufficiently strong magnetic field ensures that Γ_I is almost vertical. Achieving a flat interface growth in the presence of melt convection has been a very important objective in the processing of advanced materials [17, 32]. In order to quantify the deviation from "flat-interface growth," the standard deviation $\sigma_s(t)$ (see Eq. (18)) is calculated for the various simulations under normal as well as reduced gravity conditions. The results are illustrated in Fig. 20.

4.3.2. Effects of varying the orientation of the applied magnetic field. Considering that the electromagnetic force $\mathbf{F} \propto (\mathbf{v} \times \mathbf{e}_B) \times \mathbf{e}_B$, it is natural to expect that altering the magnetic field orientation will reveal dramatic modification in various transport phenomena. To characterize these effects, an extensive series of simulations of SbGe solidification were conducted at various inclinations of the magnetic field with $Ha = 100$. Simulations were conducted at both normal and low gravity levels in order to study independently the effects of varying the orientation of the magnetic field on the two extreme cases considered earlier.
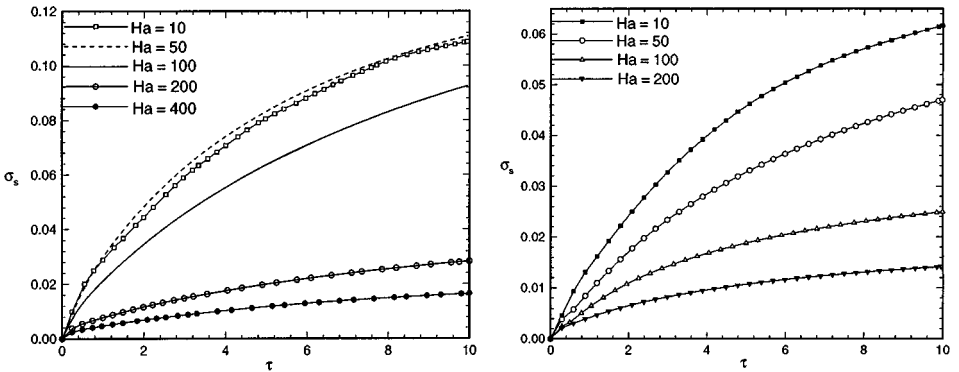

FIG. 20. The variation of the standard deviation $\sigma_s(t)$ for phase-change under the influence of a horizontally imposed external magnetic field: (a) solidification under normal gravity conditions and different Hartmann numbers and (b) solidification under reduced gravity ($g = 10^{-5} g_{earth}$) conditions and different Hartmann numbers. Notice how the interface macroscopic curvature decreases with increasing magnetic field strength.
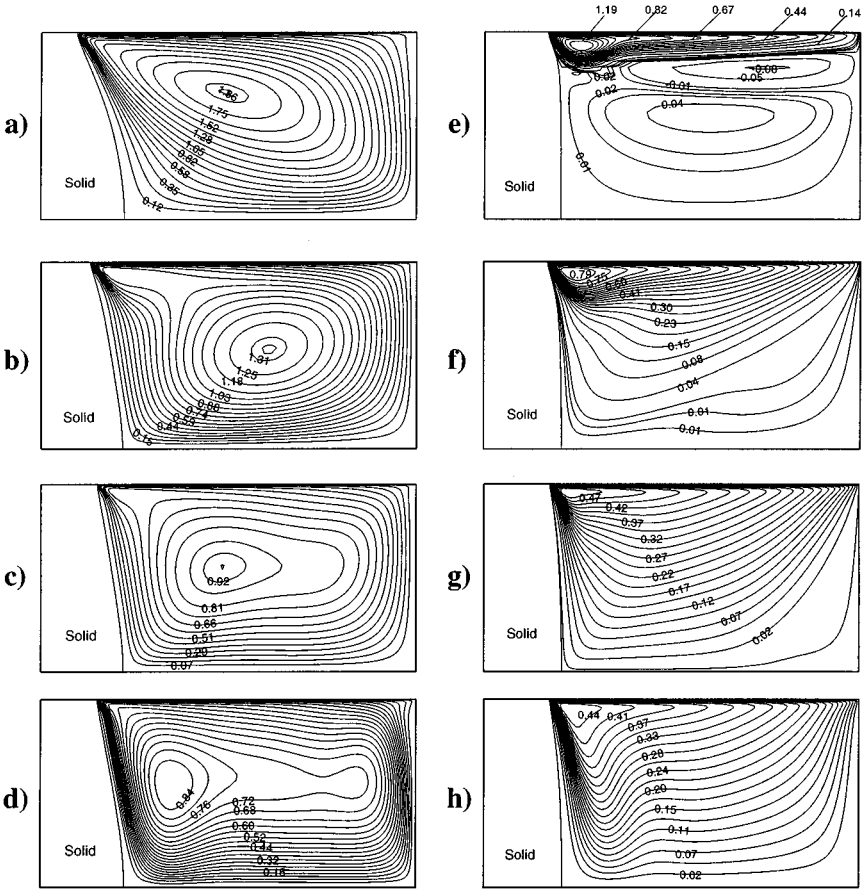
FIG. 21. Calculated contours of stream function at time $\tau = 10$ for the solidification of SbGe under the influence of an externally imposed magnetic field ($Ha = 100$) at various magnetic field orientations. Solidification under normal gravity conditions: (a) along the x-axis; (b) 30° ccw to the x-axis; (c) 60° ccw to the x-axis; and (d) along the y-axis, solidification under reduced gravity ($g = 10^{-5} g_{earth}$) conditions: (e) along the x-axis; (f) 30° ccw to the x-axis; (g) 60° ccw to the x-axis; and (h) along the y-axis.

Figure 21 shows the variety of flow patterns obtained for various magnetic field inclinations at the final time $\tau = 10$. Figures 21a–21d show the flow patterns obtained for solidification under normal gravity conditions, whereas Figs. 21e–21h show the flow patterns for solidification under very low-gravity levels ($g = 10^{-5} g_{earth}$). In both cases of solidification under normal and reduced gravity, increasing the inclination of the magnetic field appears to damp the fluid flow. Even though the change in the intensity of convection is significant, the more prominent effect of varying the orientation of the magnetic field is to alter drastically the structure of the fluid flow. In the case of solidification under normal gravity conditions, this change in structure of the flow is evident only at considerably large differences in orientation (compare Fig. 21a and Fig. 21d). However, as can be seen from Figs. 21e–21f), for the case of solidification under reduced gravity conditions, even slight variation in the orientation of the magnetic field drastically alters the orientation of the velocity vectors. This change in the flow structure affects various transport phenomena and ultimately the quality of the final crystal.

The change in the orientation of the magnetic field does not seem to have a great influence on the solidification growth velocities or the shape of Γ_I. This is in contrast to the earlier case of altering the strength of the magnetic field. A probable reason for this behavior could be the fact that the interface Γ_I is more influenced by the strength of the convection in the fluid and to a lesser degree by the exact structure of the flow in the melt.

5. SUMMARY AND CONCLUSIONS

The directional solidification of a binary alloy with an externally applied magnetic field was considered in this work. The proposed computational procedures were demonstrated with a transient simulation of solidification of antimony-doped germanium in an open-boat configuration. To assess the comparative effects of thermocapillary-, buoyancy-, and electromagnetically-driven convection, extensive series of transient calculations were performed under varying gravity levels, magnetic field strengths, and magnetic field orientations.

The reported calculations demonstrate that thermocapillary convection plays an important role in the solidification process. Under low-gravity conditions and in the absence of any external magnetic field, the melt flow develops at the free surface and slowly diffuses into the liquid. This particular phenomena leads to the local accumulation of solute and formation of various "high solute concentration spots."

Solidification under the influence of an external magnetic field is shown to produce many desirable effects. For increasing strength of the magnetic field, the intensity of the convective flow decreases and is followed by a progressive change in the overall structure of the flow. Some other interesting findings include: (i) increasing Hartmann number suppresses secondary cell formation and leads to boundary-layer formation near rigid walls; (ii) the characteristics of the final flow structure strongly depends on various factors such as orientation and strength of the applied magnetic field and gravity level; (iii) sufficiently strong magnetic fields significantly damp the convection in the melt resulting in a vertical solidification front; and (iv) application of a sufficiently strong magnetic field can greatly influence the pattern of solute distribution in the final solid.

Although restrictions related to model simplifications and computational costs limit the extent to which the present calculations provide a precise description of the behavior of a general solidification system, important trends in the various transport patterns have nevertheless been inferred. In particular, the calculations reveal the manner in which thermocapillary- and buoyancy-driven convection may interact with an applied magnetic field to influence flow development during the transient solidification of a binary alloy. In addition, the study reveals various features of the actual process which may be used in a successful design of the above process for control of the microstructure and properties of the cast product. Work in this regard is currently being pursued.

REFERENCES

1. E. L. Koschmieder, *Bénard cells and Taylor Vortices* (Cambridge Univ. Press, Cambridge, MA/New York, 1993).

2. W. Shyy, *Computational Modelling for Fluid Flow and Interfacial Transport* (Elsevier, Amsterdam/ New York, 1994).

3. D. Schwabe, Surface-tension-driven flow in crystal growth melts, in *Crystals: Growth, Properties and Applications*, edited by H. C. Freyhardt (Springer-Verlag, Berlin, 1988), Vol. 11, p. 75.

4. S. Ostrach, Fluid mechanics in crystal growth—the 1982 Freeman Scholar Lecture, *J. Fluids Eng.* **105**, 5 (1983).

5. W. E. Langlois, Buoyancy-driven flows in crystal-growth melts, *Ann. Rev. Fluid Mech.* **17**, 191 (1985).

6. H. C. Kuhlmann, *Thermocapillary Convection in Models of Crystal Growth* (Springer-Verlag, New York, 1999), p. 172.

7. T. L. Bergman, Numerical solution of double-diffusive Marangoni convection, *Phys. Fluids* **29**, 2103 (1986).

8. T. L. Bergman and S. Ramadhyani, Combined buoyancy- and thermocapillary-driven convection in open square cavities, *Numer. Heat Transfer* **9**, 441 (1986).

9. J. Metzger and D. Schwabe, Coupled buoyant thermocapillary convection, *Physico-Chem. Hydrodyn.* **10**, 263 (1988).

10. H. Ben Hadid and B. Roux, Thermocapillary convection in long horizontal layers of low-Prandtl-number melts subject to a horizontal temperature gradient, *J. Fluid Mech.* **221**, 77 (1990).

11. D. Villers and J. K. Platten, Coupled buoyancy and Marangoni convection in acetone: Experiments and comparison with numerical simulations, *J. Fluid Mech.* **234**, 487 (1992).

12. T. L. Bergman and B. W. Webb, Simulation of pure metal melting with buoyancy and surface tension forces in the liquid phase, *Int. J. Heat Mass Transfer* **33**, 139 (1990).

13. A. Liu, T. E. Voth, and T. L. Bergman, Pure material melting and solidification with liquid phase buoyancy and surface tension forces, *Int. J. Heat Mass Transfer* **36**, 411 (1993).

14. F. P. Incropera, A. H. H. Engel, and W. D. Bennon, Numerical analysis of binary solid-liquid phase change with buoyancy and surface tension driven convection, *Numer. Heat Transfer A* **16**, 407 (1989).

15. W. Shyy and M-H. Chen, Interaction of thermocapillary and natural convection flows during solidification: Normal and reduced gravity conditions, *J. Cryst. Growth* **108**, 247 (1991).

16. G. Müller and A. Ostrogorsky, Convection in melt growth, in *Handbook of Crystal Growth, Bulk Crystal Growth*, edited by D. T. J. Hurle (North-Holland, Amsterdam, 1993), Vol. 2b, Chapter 13, p. 711.

17. G. Müller, Convection and inhomogeneities in crystal growth from the melt, in *Crystals*, edited by H. C. Freyhardt (Springer-Verlag, Berlin, 1988), Vol. 12.

18. G. M. Oreper and J. Szekely, The effect of a magnetic field on transport phenomena in a Bridgman-Stockbarger crystal growth, *J. Cryst. Growth* **67**, 405 (1984).

19. S. Motakef, Magnetic field elimination of convective interference with segregation during vertical-Bridgman growth of doped semiconductors, *J. Cryst. Growth* **64**, 505 (1990).

20. D. H. Kim, P. M. Adornato, and R. A. Brown, Effect of vertical magnetic field on convection and segregation in vertical Bridgman crystal growth, *J. Cryst. Growth* **89**, 339 (1988).

21. H. Ben Hadid and D. Henry, Numerical study of convection in the horizontal Bridgman configuration under the action of a constant magnetic field. 1. Two-dimensional flow, *J. Fluid. Mech.* **333**, 23 (1997).

22. H. Ben Hadid and D. Henry, Numerical study of convection in the horizontal Bridgman configuration under the action of a constant magnetic field. 2. Three-dimensional flow, *J. Fluid. Mech.* **333**, 57 (1997).

23. S. Kaddeche, H. Ben Hadid, and D. Henry, Macrosegregation and convection in the horizontal Bridgman configuration. I. Dilute alloys, *J. Cryst. Growth* **135**, 341 (1994).

24. T. E. Tezduyar, S. Mittal, S. E. Ray, and R. Shih, Incompressible flow computations with stabilized bilinear and linear equal-order-interpolation velocity-pressure elements, *Comput. Meth. Appl. Mech. Eng.* **95**, 221 (1992).

25. T. E. Tezduyar, Stabilized finite element formulations for incompressible flow computations, *Adv. Appl. Mech.* **28**, 1 (1992).

26. R. Sampath and N. Zabaras, An object-oriented implementation of a front tracking finite element method for directional solidification processes, *Int. J. Numer. Methods Eng.* **44**(9), 1227 (1999).

27. M. E. Thompson and J. Szekely, Mathematical and physical modelling of double diffusive convection of aqueous solutions crystallizing at a vertical wall, *J. Fluid Mech.* **187**, 409 (1988).

28. R. A. Jarvis and H. E. Huppert, Solidification of a binary alloy of variable viscosity from a vertical boundary, *J. Fluid Mech.* **303**, 103 (1995).

29. J. E. Simpson and S. V. Garimella, An investigation of the solutal, thermal and flow fields in unidirectional alloy solidification, *Int. J. Heat Mass Transfer*, **41**(16), 2485 (1998).

30. K. Edwards, S. Brandon, and J. J. Derby, Transient effects during the horizontal Bridgman growth of cadmium zinc telluride, *J. Cryst. Growth* **206**, 37 (1999).

31. G. Z. Yang and N. Zabaras, The adjoint method for an inverse design problem in the directional solidification of binary alloys, *J. Comput. Phys.* **140**, 432 (1998).

32. R. Sampath and N. Zabaras, Inverse thermal design and control of solidification processes in the presence of a strong external magnetic field, *Int. J. Numer. Meth. Eng.*, in press.

33. S. R. Coriell and G. B. McFadden, Morphological stability, in *Handbook of Crystal Growth, Fundamentals: Transport and Stability*, edited by D. T. J. Hurle (North-Holland, Amsterdam, 1993), Vol. 1b, Chapter 12, p. 785.

34. C. Beckermann and R. Viskanta, Double-diffusive convection during dendritic solidification of a binary mixture, *Phys. Chem. Hydrodyn.* **10**, 195 (1988).

35. R. Moreau, *Magnetohydrodynamics* (Kluwer Academic, Dordrecht/Boston/London, 1990).

36. A. M. Bruaset, Krylov subspace iterations for sparse linear systems, in *Numerical Methods and Software Tools in Industrial Mathematics* edited by M. Daehlen and A. Tveito (Birkhauser, Boston, 1997).

37. R. Sampath and N. Zabaras, *Design and Object-oriented Implementation of a Preconditioned Stabilized Incomperssible Navier–Stokes Solver Using Equal-order-interpolation Velocity Pressure Elements*, Research Report MM-99-01 (Sibley School of Mechanical and Aerospace Engineering, Cornell University), available at http://www.mae.cornell.edu/zabaras.

38. P. M. Adornato and R. A. Brown, Convection and segregation in directional solidification of dilute and non-dilute binary alloys: Effects of ampoule and furnace design, *J. Cryst. Growth* **80**, 155 (1987).

39. R. W. Series and D.T. J. Hurle. The use of magnetic fields in semiconductor crystal growth, *J. Cryst. Growth* **113**, 305 (1991).